Tailoring the Molecular Properties with Isomerism Effect of AIEgens

Ming Chen, Junkai Liu, Feng Liu, Han Nie, Jiajie Zeng, Gengwei Lin, Anjun Qin, Mei Tu, Zikai He, Herman H. Y. Sung, Ian D. Williams, Jacky W. Y. Lam, and Ben Zhong Tang**

It is challenging to achieve precise control on the properties of organic π-functional materials to widen their practical applications. On the other hand, the study of aggregation-induced emission luminogens (AIEgens) helps achieve such goals because of inherent relationships between their luminescence behaviors and conformational variations that allow for the visual monitoring of the changes in the material properties. Inspired by this, in this work, three AIE isomers are fabricated in structures consisting of tetraphenylpyrazine and triphenylethene units with *para*-, *meta*-, and *ortho*-position linkages, respectively. The isomerism effect brings about significantly decreased luminescence efficiency, subtly blueshifted emission, basically reduced AIE effect but boosted porosity in the aggregate state as the conformation of AIEgens evolves from an extended to a folded one. Based on the distinct properties, their respective use in blue organic light-emitting diodes, nanofluorescent probes, and molecule-capturing porous crystals are investigated. This work not only achieves precise property control by using the isomerism effect of AIEgens but also provides useful information on the future design of π-conjugated materials with advanced functionalities.

1. Introduction

Organic conjugated molecules play important roles in conductance, photoelectronic conversion, luminescence, self-assembly, and multidimensional materials for their intrinsic π-conjugation and rigid structure.[1] Generally, the functions of organic conjugated molecules are controlled by molecular structure, conformation, molecular packing in the aggregate state.[2] Due to the involvement of multiple factors, more properties other than desired ones are usually obtained to lead to unexpected performance of the designed materials. For example, the semiconducting layers of organic field effect transistors often consist of organic conjugated molecules with planar structures. The close packing of the planar molecules benefits the overlap of π-electron cloud between the adjacent molecules, which dramatically improves the mobility of the materials. However, the recombination of excitons in device operation contributing to luminescence or heat is still inevitable.[3] On the contrary, π-π stacking in organic emitters should be strongly prohibited because it is a notorious cause for emission quenching in the aggregate state.[4] To solve such problem, various methods such as designing molecules with twisted or branched architectures and covalently hanging them on rigid cubes have been adopted

Dr. M. Chen, F. Liu, Prof. M. Tu
College of Chemistry and Materials Science
Jinan University
Guangzhou 510632, China
Dr. M. Chen, J. Liu, Dr. H. H. Y. Sung, Prof. I. D. Williams, Dr. J. W. Y. Lam, Prof. B. Z. Tang
Department of Chemistry
Hong Kong Branch of Chinese National Engineering Research Center for Tissue Restoration and Reconstruction
Institute for Advanced Study
Department of Chemical and Biological Engineering
Division of Life Science
State Key Laboratory of Molecular Neuroscience and Institute of Molecular Functional Materials
The Hong Kong University of Science and Technology
Clear Water Bay, Kowloon, Hong Kong, China
E-mail: tangbenz@ust.hk
The ORCID identification number(s) for the author(s) of this article can be found under https://doi.org/10.1002/adfm.201903834.
Dr. M. Chen, J. Liu, Dr. J. W. Y. Lam, Prof. B. Z. Tang
HKUST-Shenzhen Research Institute
No.9 Yuexing 1st RD, South Area, Hi-Tech Park, Nanshan 518057, China
Dr. H. Nie, J. Zeng, G. Lin, Prof. A. Qin, Prof. B. Z. Tang
Center for Aggregation-Induced Emission
SCUT-HKUST Joint Research Institute
State Key Laboratory of Luminescent Materials and Devices
South China University of Technology
Guangzhou 510640, China
E-mail: msqinaj@scut.edu.cn
Prof. Z. He
School of Science
Harbin Institute of Technology Shenzhen
HIT Campus of University Town of Shenzhen
Nanshan, Shenzhen 518055, China

DOI: 10.1002/adfm.201903834

© 2019 WILEY-VCH Verlag GmbH & Co. KGaA, Weinheim

but have achieved with only limited success.[5] Most often, the π–π stacking cannot be overcome radically by suppressing the molecular aggregation to exempt influence on the emission efficiency. Thus, it is of great significance, yet a challenge, to regulate the molecular properties precisely by reading the molecular information comprehensively and rationally.

Conjugated luminogens with aggregation-induced emission (AIE) characteristics have attracted considerable attention for their wide applications in organic light-emitting diodes (OLEDs), fluorescent sensors, bioimaging, etc.[6] The intrinsic characteristic of AIE luminogens (AIEgens) is their twisted and flexible molecular conformation, which makes them to emit faintly in solution due to the active intramolecular motions but show remarkably enhanced emission in the aggregate state due to the restriction of such motions.[7] The nonplanar structures of AIEgens also endow them with tunable structural transformability because of the loose molecular packing in the aggregate state which provides more free space for conformational change. For example, our group prepared hyperbranched polymers constructed from AIE unit of tetraphenylethene. The polymers seem rigid but actually can be compressed like "spring" under external stimuli.[8] Moreover, we and other groups reported AIEgen-based soft porous crystals, which can encapsulate organic small molecules by virtue of their porous framework determined by stereo and flexible conformation of AIEgens, their intermolecular interactions, etc.[9] Recently, we also designed AIEgens with near-infrared absorption that exhibited controllable intramolecular motions in the aggregate state. Such property equilibrates luminescence and heat formation due to the excited-state energy dissipation, making these AIEgens as promising multifunctional biomedical agents in combination of fluorescence imaging, photoacoustic imaging, and photothermal therapy.[10] Notably, AIEgens are not only competent in strong solid-state luminescence but also closely related to plentiful conformational changes that influence the solid-state properties. Thus, it is interesting to tailor the molecular properties by studying AIEgens as the guideline, which will assist further design of materials with desired properties.

With these in mind, in this work, we prepared three conjugated isomers by connecting tetraphenylpyrazine (TPP) and triphenylethene (TPE) at the *para*-, *meta*-, and *ortho*-position, respectively (**Figure 1**). These isomers show AIE features inherited from TPP and TPE.[11] When the conformation of these isomers evolves from a linear to a folded one, the emission was weakened gradually because of reduced molecular conjugation and decreased restriction of intramolecular motion due to the loose intermolecular packing. On the other hand, the molecular porosity increases, as revealed by the formation of porous crystals of *ortho*-isomer with defined nanocavities and nanochannels easily that can capture guest molecules like dichloromethane (DCM) and tetrahydrofuran (THF). The potential applications of these AIEgens as luminescent materials (e.g., OLED and nanoprobes) were also presented.

2. Results and Discussion

2.1. Synthesis, Characterization, and Thermal Properties of AIE Isomers

The AIE isomers, namely TPP-*p*-TPE, TPP-*m*-TPE, and TPP-*o*-TPE, were synthesized by Suzuki coupling of Br- or boric acid ester-substituted TPP or TPE intermediates using $Pd(PPh_3)_4$ as catalyst (Figure 1 and Scheme S1, Supporting Information). The finial products were carefully purified using column chromatography and their structures were fully characterized by ^1H and ^{13}C NMR and high resolution mass spectroscopies with satisfactory data corresponding to their structures

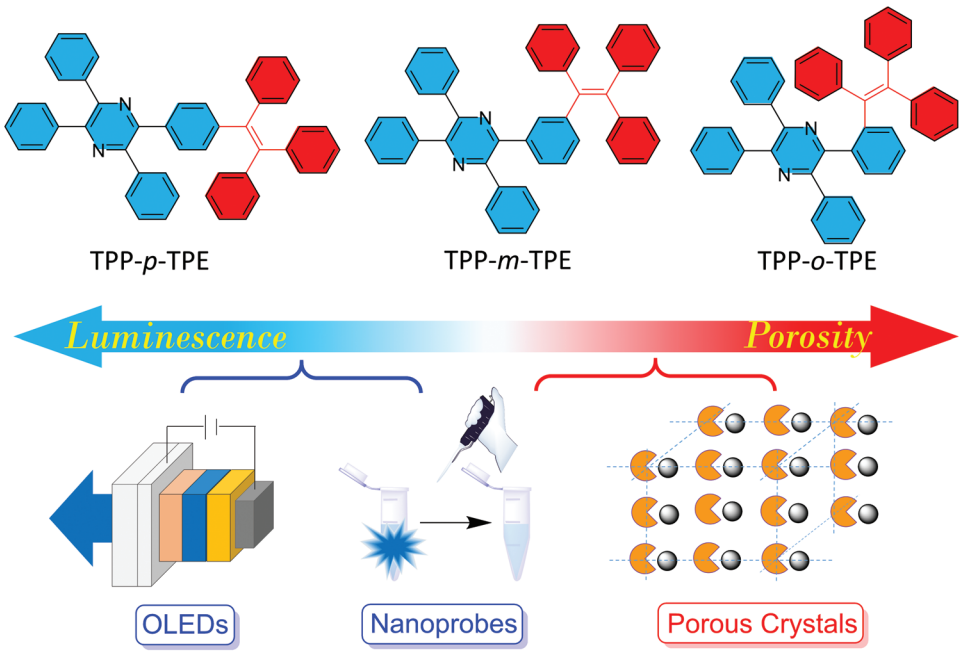

Figure 1. Schematic illustration of functionalities tuned by the isomerism effect of AIEgens.

© 2019 WILEY-VCH Verlag GmbH & Co. KGaA, Weinheim

(Figures S1–S23, Supporting Information). Thermogravimetric analysis (TGA) shows that AIE isomers show 5% weight loss at temperatures of 338, 309, and 295 °C, respectively, suggestive of a good thermal stability (Figure S24, Supporting Information). Analysis by differential scanning calorimetry (DSC) reveals that TPP-*m*-TPE and TPP-*o*-TPE show a similar glass transition temperature (T_g) of 110 °C, while no T_g is found for TPP-*p*-TPE (Figure S25, Supporting Information). Such difference is probably attributed to the varied molecular conformation and molecular packing model of the isomers in the aggregate state.

2.2. Optical Properties

Since the isomers are composed of typical AIE units of TPP and TPE with *para*-, *meta*-, and *ortho*-linkages, they are anticipated to show different photophysical properties. We first studied the UV absorption spectra of the isomers in THF (**Figure 2**). TPP-*p*-TPE, TPP-*m*-TPE, and TPP-*o*-TPE exhibit an absorption maximum at 350, 336, and 332 nm, respectively, due to the π–π^* transition of the chromophores. These values are similar to that of TPP (338 nm), demonstrating that the TPP moiety play a crucial role in the absorption of the molecules.[11a] Because the molecular conjugation is weakened from the conformation of the molecules changed from extended in *para*-isomer to folded in *ortho*-isomer, their absorption maximum blue-shifts accordingly. Interestingly, TPP-*o*-TPE shows a molar absorptivity of 4.28×10^4 L mol^{-1} cm^{-1}, which is close to TPP-*p*-TPE (4.26×10^4 L mol^{-1} cm^{-1}) but larger than that of TPP-*m*-TPE (3.22×10^4 L mol^{-1} cm^{-1}) in spite of its much folded conformation. It is probably due to the another intramolecular through-space charge transfer transition, which takes places from TPE to TPP units as they locate adjacently in space in the folded conformation, therefore increasing the probability of transition.[12]

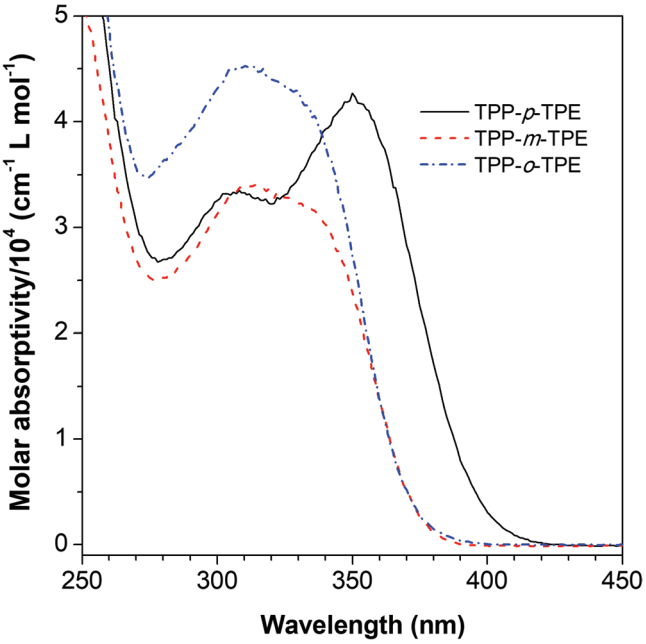

Figure 2. UV–vis spectra of TPP-*p*-TPE, TPP-*m*-TPE, and TPP-*o*-TPE in THF [dye] = 10×10^{-6} M.

The photoluminescence (PL) of the isomers was then studied in THF/water mixtures with different water fractions (f_w) (**Figure 3**). All the molecules exhibit only noisy signals with no discernible peak maximum in diluted THF solution (10×10^{-6} M). The emission remains weak when up to 60 vol % of water was added to the THF solutions. Afterward, intense emission signals are recorded. This is because the luminogens are molecularly dissolved in THF and the vigorous intramolecular motions in solution dissipate the excited-state energy nonradiatively. However, nanoaggregates form in the presence of a large amount of water, which restricts such motion and allow the excitons to relax radiatively. The absolute quantum yields (QYs) of TPP-*p*-TPE, TPP-*m*-TPE, and TPP-*o*-TPE in films measured by an integrating sphere are 54.2%, 34.2%, and 5.0%, respectively while no reliable values can be collected in the solution state due to the weak intensity (**Table 1**). The much higher QYs in films than in THF and the results from PL spectra both confirm that these isomers are AIE-active. Both TPP and TPE are well-known AIEgens, melding them together certainly will produce new luminogens with property inherited from both the AIE parent units.

The TPP-*p*-TPE, TPP-*m*-TPE, and TPP-*o*-TPE films emit at 477, 468, and 454 nm, and show emission colors from sky-blue to deep blue. These results are consistent with those of nanoaggregates in THF/water mixtures (Figure S26, Supporting Information). The bluer emission in the film state may attribute to the decreased molecular conjugation due to the conformation change. The emission properties of AIE isomers are basically the same as that of tetraphenylethene.[13] However, they show some difference in AIE effect. For example, the α_{AIE} values (defined as the ratio between the PL intensity of the molecules in THF/water mixtures with f_w = 95% and THF) of TPP-*p*-TPE, TPP-*m*-TPE, and TPP-*o*-TPE are calculated to be 249, 275, and 47, respectively. Since the isomers are nonemissive in solution, the AIE behavior is often determined by the luminescent behavior in the aggregate state. Thus, the excited-state decay of the films was further studied by the formula of $k_r = \Phi_F/\tau$ and $k_{nr} = (1 - \Phi)/\tau$, where k_r and k_{nr} are the radiative and nonradiative decay rates, and Φ_F and τ are the absolute quantum yield and excited-state lifetime, respectively. The calculated k_r of the isomers in the films state are 2.27×10^8, 0.85×10^8, and 0.19×10^8 S^{-1}, respectively, indicating that the radiative transition is influenced remarkably by the molecular conjugation. On the other hand, the k_{nr} of TPP-*p*-TPE (1.92×10^8 S^{-1}) and TPP-*m*-TPE (1.64×10^8 S^{-1}) are relatively close and are lower than that of TPP-*o*-TPE (3.57×10^8 S^{-1}) (Figure S27 in the Supporting Information and Table 1). This is due to the much folded conformation of TPP-*o*-TPE, which makes its molecules to pack loosely in the aggregate state to introduce free volume to promote molecular motions. Nevertheless, the isomerism effect exerts stronger influence on the radiative transition than the nonradiative transition of the AIE isomers.

The S_0 geometry of the AIE isomers optimized by B3LPY/6-31(d) level reveals that all the molecules adopt a twisted structure (**Figure 4**). TPP-*p*-TPE shows a relatively more extended conformation, whereas TPP-*m*-TPE and TPP-*o*-TPE are much folded because their TPP and TPE units are located much adjacently in space. The highest occupied molecular orbital (HOMO) and the lowest unoccupied molecular orbital (LUMO) of TPP-*p*-TPE

© 2019 WILEY-VCH Verlag GmbH & Co. KGaA, Weinheim

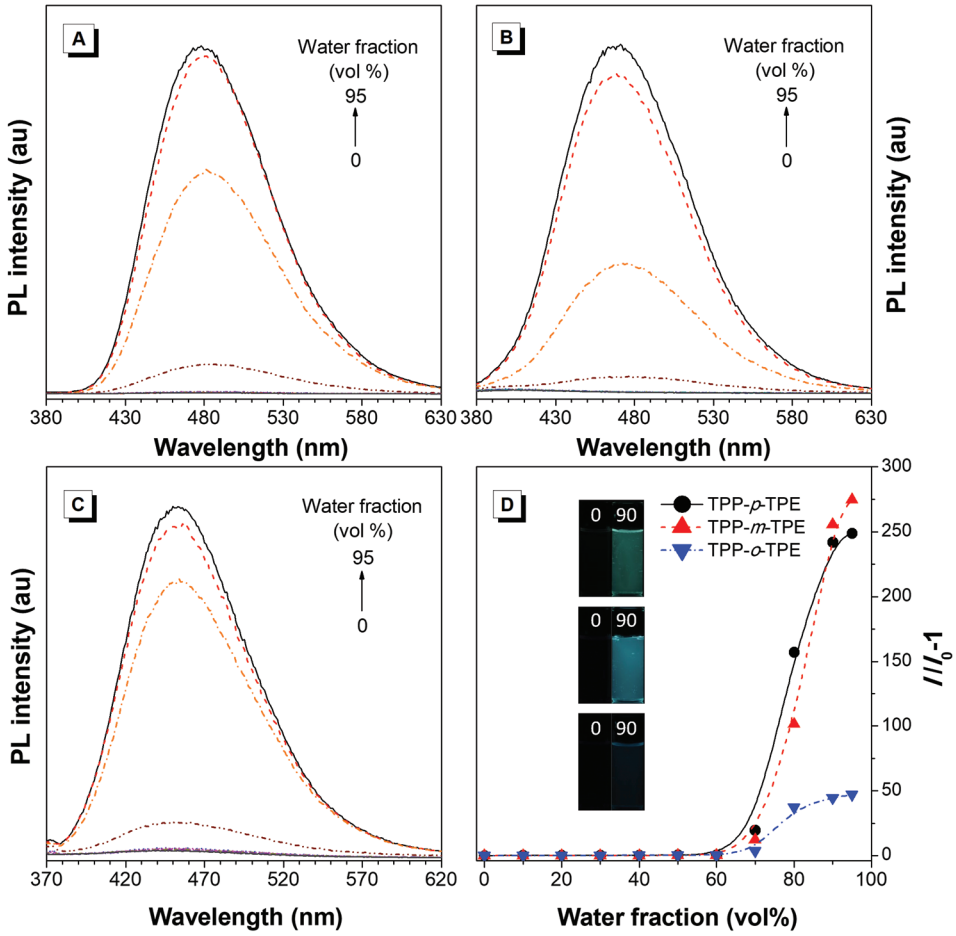

Figure 3. PL spectra of A) TPP-*p*-TPE, B) TPP-*m*-TPE, and C) TPP-*o*-TPE in THF/water mixtures with different water fractions (f_w). Dye concentration = 10×10^{-6} M; excitation wavelengths = 350, 336, and 332 nm, respectively. D) Plot of relative PL intensity ($I/I_0 - 1$) versus the composition of THF/water mixtures of AIE isomers, where I_0 = PL intensity in pure THF solution. Inset: fluorescent photographs of TPP-*p*-TPE, TPP-*m*-TPE, and TPP-*o*-TPE (from top to bottom) in THF (left) and THF/water mixtures (right) with f_w = 90%.

are contributed by orbitals of all units, while in TPP-*m*-TPE and TPP-*o*-TPE, the orbitals of the HOMO and LUMO are mainly contributed by TPE and TPP, respectively. Such theoretical analysis further confirms that TPP- *p*-TPE shows a better conjugation than TPP-*m*-TPE and TPP-*o*-TPE to contribute greater radiative transition.

Table 1. Photophysical properties of the AIE isomers.

	λ_{abs} [nm]	λ_{em} [nm]	Φ_F [%]	τ [ns]	k [10^8 S^{-1}]	k_{nr} [10^8 S^{-1}]
TPP-*p*-TPE	350	477	54.2	2.39	2.27	1.92
TPP-*m*-TPE	336	468	34.2	4.01	0.85	1.64
TPP-*o*-TPE	332	454	5.0	2.66	0.19	3.57

Abbreviation: λ_{abs}: absorption maximum in THF; λ_{em}: emission maximum in films; Φ_F: fluorescence quantum yields of films measured by an integrating sphere; τ: fluorescence lifetime of films; k_r: rate of radiative decay of films = Φ_F/τ; k_{nr}: rate of nonradiative decay of films = $(1 - \Phi_F)/\tau$. The films are obtained by coating the THF solution of molecules onto quartz sheet followed by removing the solvent by evaporation.

2.3. Organic Light-Emitting Diodes

Thanks to the high PL efficiency of TPP-*p*-TPE and TPP-*m*-TPE in the film state, they are promising to serve as light-emitting layers of blue OLEDs. Before device fabrication, their energy levels are first evaluated. The HOMO and LUMO energy

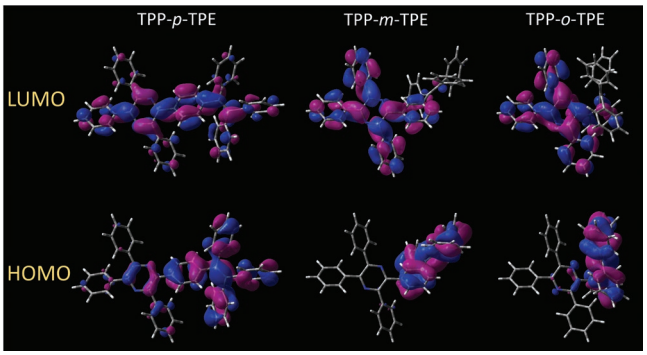

Figure 4. Electron cloud distributions of the HOMO and LUMO based on S_0 geometry of AIE isomers optimized by B3LPY/6-31(d) level.

© 2019 WILEY-VCH Verlag GmbH & Co. KGaA, Weinheim

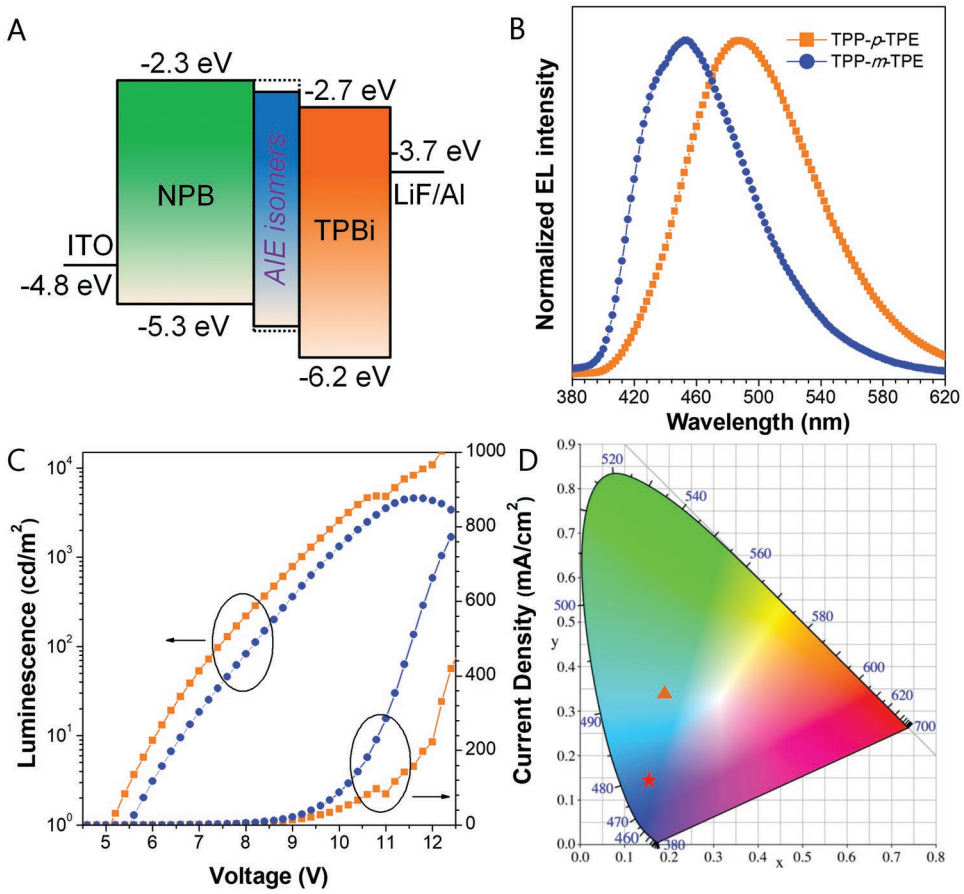

Figure 5. A) The schematic energy level diagram of the materials used in the OLED devices. B) EL spectra of the devices. C) Plot of luminance and current density with the applied voltage of devices. D) CIE coordinates of the devices, where the triangle and the star represent TPP-*p*-TPE- and TPP-*m*-TPE-based devices, respectively.

levels of TPP-*p*-TPE and TPP-*m*-TPE are deduced as –5.58 and –5.62 eV, and –2.46 and –2.30 eV, respectively, by cyclic voltammetry and UV spectroscopy (Figure S28, Supporting Information). Considering the importance of energy level matching in device design, commercial *N,N′*-di(1-naphthyl)-*N,N′*-diphenylbenzidine (NPB) and 1,3,5-tri(1-phenyl-1*H*-benzo[d]imidazol-2-yl)phenyl (TPBi) are chosen as hole-transporting and electron-transporting layers, respectively. Besides, ITO, Al, and LiF are separately used as anode, cathode and electron-injecting layer. This forms typical triple-layer electroluminescence (EL) devices with a configuration of ITO/NPB (60 nm)/AIE isomer (20 nm)/ TPBi (40 nm)/LiF (1 nm)/Al (**Figure 5**A).

The TPP-*p*-TPE-based device (device I) turns on at 5.1 V and shows maximum luminance (L_{max}), current efficiency (η_c), powder efficiency (η_p) and external quantum efficiency (η_{ext}) of 18 431 cd m^{-2}, 6.12 cd A^{-1}, 3.07 lm W^{-1}, and 2.74%, respectively. The device displays sky-blue emission at 488 nm with a Commission Internationale de L'Eclairage (CIE) coordinate of (0.19, 0.34) (Figure 5B–D and **Table 2**). Such result is comparable to many AIEgen-based OLEDs with sky-blue emission. However, its emission color is much redder and still conflicts with blue light for practical application. In contrast, device II fabricated using TPP-*m*-TPE as luminescent layer shows a deep-blue emission at 454 nm. The CIE coordinate is (0.16, 0.15). Thus, the emission color is much purer than the former.[14] Nevertheless, its performance is poorer. For example, its L_{max}, η_c, and η_p are measured to be 4571 cd m^{-2}, 1.65 cd A^{-1}, and 0.72 lm W^{-1}, respectively, which are much lower than those of device I. Besides, the η_{ext} is almost half of that of device I. It is understandable as TPP-*m*-TPE possess a lower quantum yield than TPP-*p*-TPE in the film state because of its shorter conjugation length caused by the more crooked molecular conformation. On the other hand, such a molecule cannot pack well in the aggregate state due to the steric effect of its V-shaped structure. Because carrier's transportation is through hopping between its adjacent molecules in the emitting layer,[15] the loose packing of TPP-*m*-TPE will lessen its charge transport capacity to collectively deteriorate the device performance. These results imply that the emission wavelength of a compound can be tuned to meet desirable OLED application by isomerism strategy, but the best device performance is achieved in molecules with good conjugation.

2.4. Nanofluorescent Probes

The AIE isomers exhibit varied luminescent behaviors and are likely to form nanoaggregates in THF/water mixtures with different morphologies caused by the isomerism effect. Since

© 2019 WILEY-VCH Verlag GmbH & Co. KGaA, Weinheim

Table 2. EL performances of the devices.

	λ_{EL} [nm]	V_{on}[V]	L_{max} [cd m^{-2}]	η_c [cd A^{-1}]	η_p [lm W^{-1}]	EQE [%]	CIE [x, y]
TPP-*p*-TPE	488	5.1	18341	6.12	3.07	2.74	(0.19, 0.34)
TPP-*m*-TPE	454	5.5	4571	1.65	0.72	1.41	(0.16, 0.15)

Abbreviation: λ_{EL}: emission maximum of the EL spectra; V_{on}: turn-on voltage; L_{max}, η_c, η_p, EQE: maximum values of luminescence, current efficiency, power efficiency, and external quantum efficiency of the devices, respectively; CIE (x, y): CIE coordinate at 1000 cd m^{-2}.

AIE nanoaggregates are highly emissive and have found potential applications as fluorescent sensors, how does the molecular isomerism affect the detection results? To answer this question, we first evaluated their detection behavior for aromatic explosives because these analytes are electron-deficient and interact readily with most fluorescent molecules to alter their PL. Herein, we used 2,4,6-trinitrophenol (picric acid, PA) as model explosive for study due to its commercial availability. **Figure 6**A–C shows the PL spectra of the nanoaggregates of the AIE isomers formed in THF/water mixtures with f_w = 90% in the presence of PA. With an increase of the amount of PA added, the PL of the molecules decreases progressively. The fluorescence quenching can be clearly discerned at a PA concentration of as low as 5×10^{-6} M and the PL signals are almost lost at a PA concentration of 300×10^{-6} M.

Remarkably, the Stern-Volmer plots of $I/I_0 - 1$ versus [PA] show overall upward bent curves instead of linear ones (Figure 6D). This means the PL quenching becomes efficient as the analyte concentration increases, indicative of a superamplification effect for PA detection. It is probably because each PA molecule can have more probability to interact with AIEgens in the surroundings once PA is encapsulated into the probe. It is worth noting that TPP-*o*-TPA shows a stronger emission quenching than TPP-*m*-TPE at high quencher concentration, in spite of its much weaker PL in nanoaggregates. It is mostly due to the porous structure of the nanoparticle

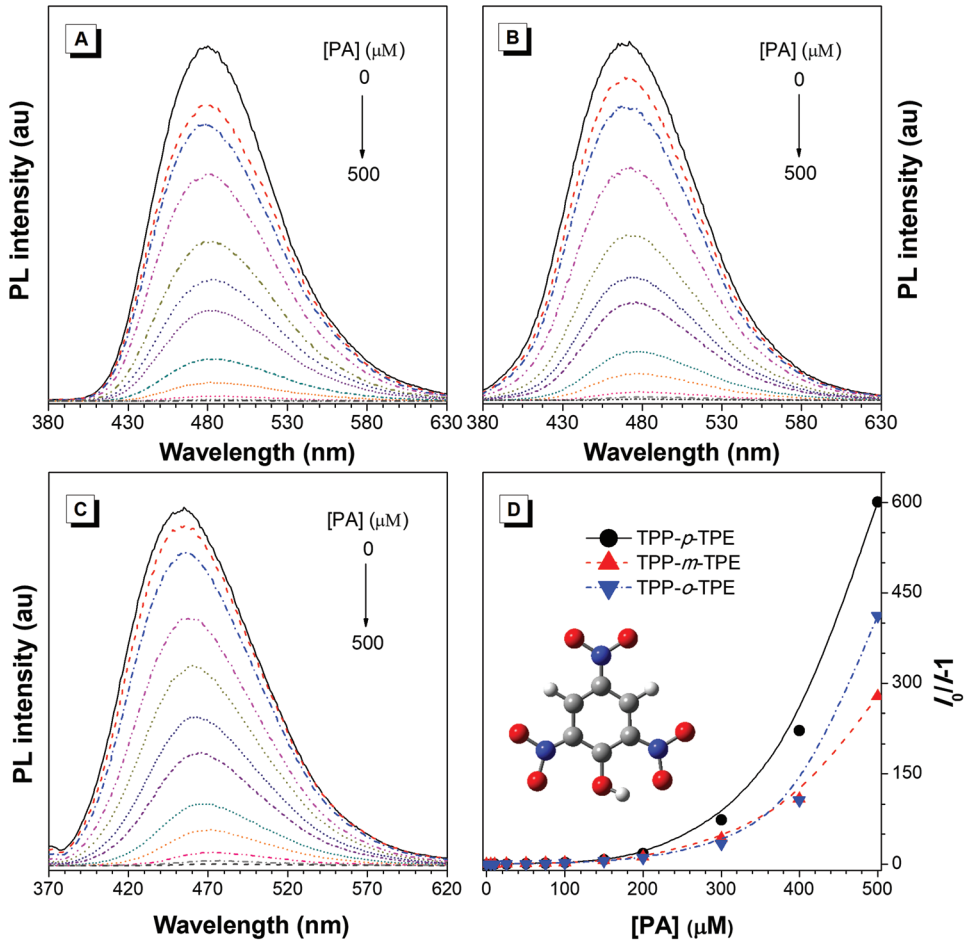

Figure 6. PL spectra of A) TPP-*p*-TPE, B) TPP-*m*-TPE, and C) TPP-*o*-TPE nanoaggregates formed in THF/water mixtures with f_w = 90% in the presence of PA with different concentrations. Dye concentration = 10×10^{-6} M; excitation wavelengths = 350, 336, and 332 nm, respectively. D) Plots of $I_0/I - 1$ versus PA concentration, where I = peak intensity and I_0 = peak intensity at [PA] = 0×10^{-6} M. Inset: chemical structure of PA.

© 2019 WILEY-VCH Verlag GmbH & Co. KGaA, Weinheim

suspension generated by the loose packing of TPP-*o*-TPE molecules upon aggregation. The porosity of TPP-*o*-TPE aggregates facilitates the interaction of the probe with analyte to improve its sensitivity at high quencher concentration. However, its quenching efficiency is somewhat smaller than that of TPP-*p*-TPE. This is because the stronger Lewis acid-base interactions are inclined to take place between PA and AIE isomers with better conjugation, which helps to quench the emission. The two effects are competitive in determining the probe behavior.[16]

On the other hand, careful examination of the Stern-Volmer plots depicts that linear relationships exist at PA concentration from 0 to 75×10^{-6} M with similar quenching constants of 25 457, 25 459, and 19 351 M^{-1}, respectively (Figure S29, Supporting Information). This indicates that the morphologies of the nanoaggregates and Lewis acid-base interactions caused by isomerism effect exert less influence on the sensitivity of PA sensors at Low PA concentration than at high quencher concentration.

More specifically, the PL decay curves of nanoparticle suspensions treated with PA of 0, 50×10^{-6}, and 150×10^{-6} M are investigated. Before PA addition, lifetimes of 2.81 ns, 3.79 ns and 2.29 ns, respectively are deduced, whose values remain almost unchanged during the PA titration process (Figure S30, Supporting Information). The independence of the lifetime of nanoaggregates on the PA concentration indicates that the quenching mechanism is ascribed to a static quenching model, in which the electron transition takes place from the ground state of AIEgen to the excited-state of PA to form nonluminescent complexes in the ground state. The shift in UV absorption spectra of probe in the presence of PA further confirms the formation of such complexes (Figure S31, Supporting Information).[17] In static quenching, the lifetime of the probe will not be affected because those luminogens which are not complexed will have normal excited-state properties. Thus, the fluorescence quenching is caused neither by photoinduced electron transfer nor energy transfer because no excited-state behavior of AIEgen is participated in the process. In other words, the PL efficiency of the AIE nanoaggregates determined by the isomerism effect will subtly influence the quenching process for PA detection.

Next, we investigated whether the fluorescent probes based on AIE isomers could respond to the metal ion of ruthenium(III) (Ru^{3+}) because it interact readily with fluorescent molecules with heteroatoms as reported.[18] Similarly, the nanoaggregates of AIEgens formed in THF/water mixture with f_w = 90% are used as probes. The emission of TPP-*p*-TPE, TPP-*m*-TPE, and TPP-*o*-TPE quenches progressively with gradual addition of Ru^{3+} (**Figure 7**A–C). The responses can be clearly recorded at a Ru^{3+} concentration of as low as 1×10^{-6} M. The Stern-Volmer plots of $I/I_0 - 1$ versus [Ru^{3+}] are nearly linear until the Ru^{3+} concentration reaches 12×10^{-6}, 8×10^{-6}, and 16×10^{-6} M for TPP-*p*-TPE, TPP-*m*-TPE, and TPP-*o*-TPE, respectively. Afterward, plateaus are reached. At these concentrations, the PL intensity of the isomers decreases by about 79%, 67%, and 65%, respectively (Figure 7D). These results are different from previous AIEgen-based Ru^{3+} sensors, which show remarkable quenching behavior but no observable plateau.[19]

The quenching constants of these probes at low Ru^{3+} concentration are 343 535, 28 5062, and 137 893 M^{-1}, respectively, determined from the slopes of the linear curves (Figure S32, Supporting Information). The gradual decline in quenching constant seems to indicate that the quenching efficiency is closely related to the PL efficiencies of the nanoaggregates. Besides, the quenching extent of TPP-*m*-TPE nanoaggregates is nearly the same as that of TPP-*o*-TPE, though the response of the later is much slower. This demonstrates that the porosity of AIE isomers may play another role in affecting the quenching behavior.

Different from PL lifetime study of PA detection, the lifetime of the AIE nanoparticles decreases obviously when titrated with Ru^{3+}. The lifetimes of TPP-*p*-TPE, TPP-*m*-TPE, and TPP-*o*-TPE were recorded as 0.62, 1.80, and 1.39 ns, respectively, in the presence of 10×10^{-6} M of Ru^{3+}, which were much lower than their initial values without quenchers (2.81, 3.79, and 2.29 ns, respectively) (Figure S33, Supporting Information). The changes of lifetime manifests that a dynamic (collisional) quenching model dominates the mechanism of Ru^{3+} detection.[20] Since this mechanism requires a close contact of the excited fluorophores with the analytes, the quenching effect is thus related to Dexter energy transfer because such a short distance may help electron exchange between the donor and the acceptor. The mechanism is different from the previous Ru^{3+} probe with quenching behavior based on AIEgens because Ru^{3+} only act as acceptor here for energy transfer.[19] However, the fluorescence resonance energy transfer (FRET) is almost impossible to happen, though the quenching behavior is seemingly related to the PL intensities of probes. It is because FRET is a long-distance interaction between donor and acceptor. If FRET exists, it will help to quench all the emissions by long-distance action. Since the plateau occurs, there must have some AIEgens which are not influenced by Dexter energy transfer due to distance limit to give the emissions. The spectral overlap between the absorption of Ru^{3+} and the emissions of probes is beneficial for Dexter energy transfer process. (Figure S34, Supporting Information).

For probes fabricated with TPP-*p*-TPE, the Ru^{3+} should be encapsulated more compactly and homogeneously into the nanoparticles, which can facilitate the interaction between probe and analytes. Whereas, in TPP-*m*-TPE and TPP-*o*-TPE-based probes, more Ru^{3+} are gathering in the cavities of probes, thus possessing fewer opportunities to participate in Dexter energy transfer. Nevertheless, because TPP-*o*-TPE shows the best porosity, the Ru^{3+} is very likely to diffuse along the 3D voids in the probe, which can explain why TPP-*o*-TPE shows similar maximum quenching extent with TPP-*m*-TPE as probes but reaches the plateau at a higher quencher concentration.

Besides, the selectivity of Ru^{3+} detection is also evaluated in the presence of other metal ions. As shown in Figures S35–37 (Supporting Information), addition of other metal ions, such as Ag^{+}, Cd^{2+}, Cu^{2+}, Fe^{2+}, Fe^{3+}, Ir^{3+}, Mg^{2+}, Ni^{2+}, Pb^{2+}, Rh^{3+}, and Zn^{2+}, exerts negligible changes in the PL spectra of TPP-*p*-TPE, TPP-*m*-TPE, and TPP-*o*-TPE-based probes, indicative of a good selectivity toward Ru^{3+}, which is independent on the isomerism effect.

© 2019 WILEY-VCH Verlag GmbH & Co. KGaA, Weinheim

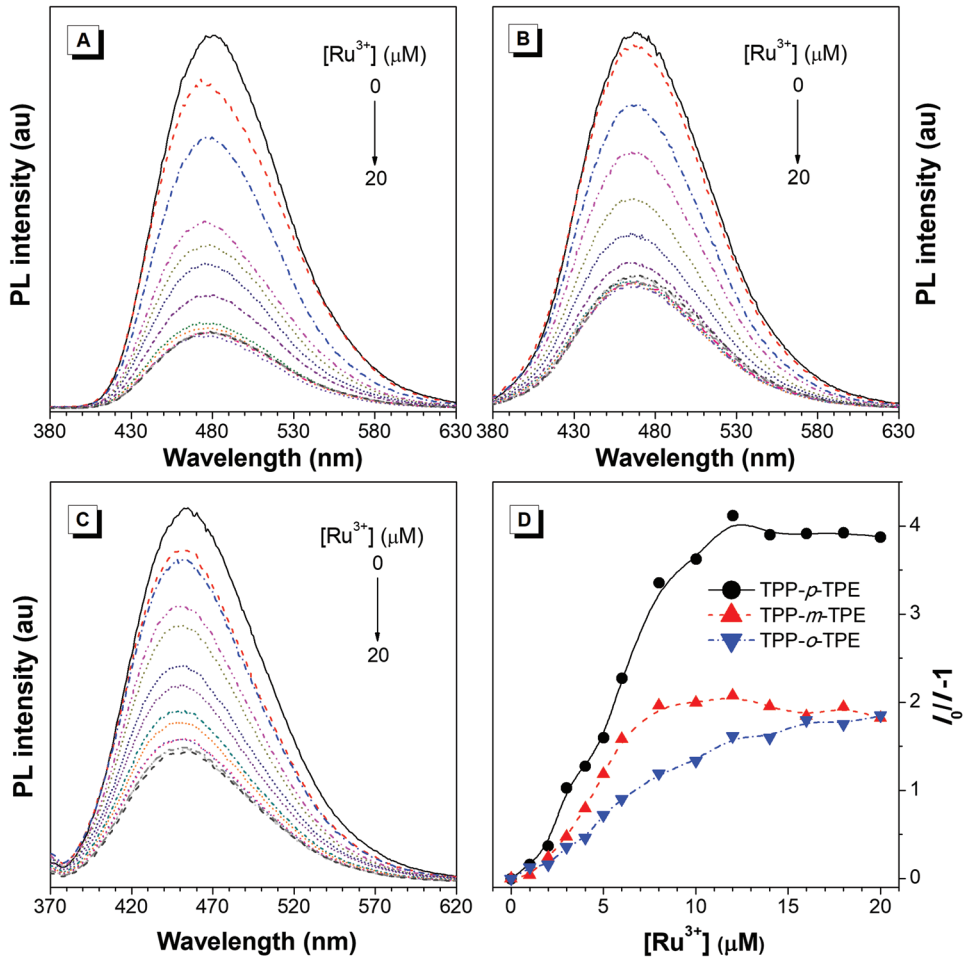

Figure 7. PL spectra of A) TPP-*p*-TPE, B) TPP-*m*-TPE, and C) TPP-*o*-TPE nanoaggregates formed in THF/water mixtures with $f_w = 90\%$ in the presence of Ru^{3+} with different concentrations. Dye concentration = 10×10^{-6} M; excitation wavelengths = 350, 336, and 332 nm, respectively. D) Plots of $I_0/I - 1$ versus Ru^{3+} concentration, where I = peak intensity and I_0 = peak intensity at $[Ru^{3+}] = 0 \times 10^{-6}$ M.

2.5. Porous Crystals

Studies on the X-ray crystal structures of the AIE isomers provide further insight into the molecular information in the aggregate state. Fortunately, three crystals of TPP-*p*-TPE and TPP-*o*-TPE suitable for X-ray analysis were obtained in mixed solvent of $CHCl_3$/hexane, CH_2Cl_2/methanol and THF/methanol, respectively (**Figure 8**A–C). We also tried to grow single crystals of TPP-*m*-TPE but only obtained cotton-like powders even various methods had been adopted, which is possibly due to its V-shaped conformation that is not favorable for ordered molecular packing. The crystal structure of TPP-*p*-TPE shows an extended conformation as a whole while the phenyl rings at the periphery of molecules still twist against the central pyrazine ring and the double bond. By comparison, the conformation of TPP-*o*-TPE is highly folded as the TPE unit is linked to the TPP unit at *ortho*-position. Such geometrical structures of AIE isomers are well in accordance with the results obtained by the theoretical simulation.

The stretching conformation of TPP-*p*-TPE makes them easy to pack well in the aggregate state. As shown in Figure 8D, multiple intramolecular C—H...π interactions with short distance of 2.80 and 3.35 Å are found between C—H bonds and adjacent phenyl rings, which assists in locking the molecular conformation. Besides, strong C—H...π interaction with a distance of 2.77 Å and C—H...N interaction with a distance of 2.89 Å exist between molecules, which facilitate their close packing in the crystal lattice. Both factors induce the formation of compact aggregate-state structure without obvious cavities (Figure 8G). In contrast, except the intramolecular C—H...N hydrogen bond formed between the C-H bond of the TPE units and the N atom of the pyrazine ring, no other interactions are found in TPP-*o*-TPE crystals (Figure 8E,F). The bonding distances (2.63 and 2.68 Å) are shorter than those in TPP-*p*-TPE, indicative of strong interactions that help to self-lock the folded conformation of TPP-*o*-TPE. Interestingly, the fold conformation of TPP-*o*-TPE also provides effective free volume for molecule capture. For example, during the single crystal culture, the solvent molecules of DCM and THF are easy to enter the free space and generate complexes with host in a molar ratio of 1:1. Notably, the DCM molecule captured by TPP-*o*-TPE shows a blurred structure, especially for the two chlorine atoms, which exhibit additional trace beyond the original structure (Figure S38, Supporting Information). This is because the

© 2019 WILEY-VCH Verlag GmbH & Co. KGaA, Weinheim

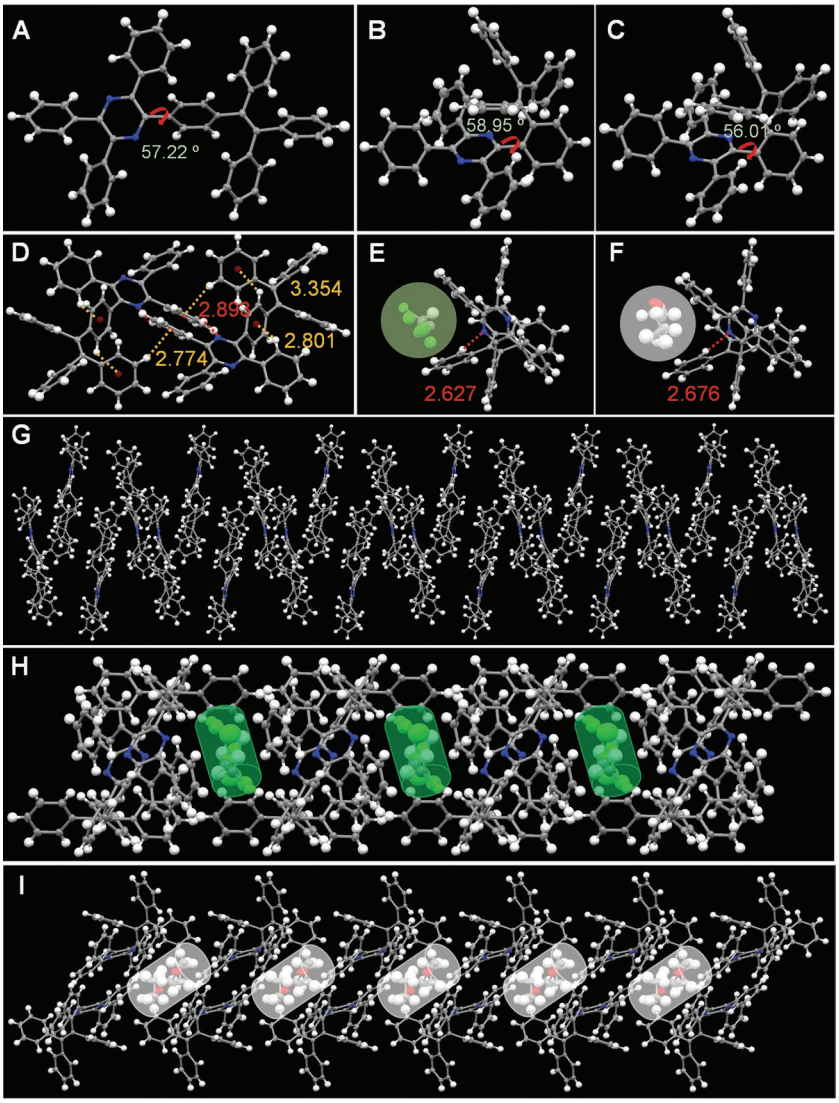

Figure 8. Crystal structures of A) TPP-*p*-TPE and TPP-*o*-TPE grown from B) CH_2Cl_2/methanol and C) THF/methanol. D) Multiple intermolecular and intramolecular interactions in crystals of TPP-*p*-TPE with indicated distances (Å). Intramolecular C—H...N interaction of TPP-*o*-TPE crystals grown from E) CH_2Cl_2/methanol and F) THF/methanol with indicated distances (Å) and their complexes with CH_2Cl_2 and THF. G) Molecular packing of TPP-*p*-TPE crystals. Porous crystals of TPP-*o*-TPE for capturing H) CH_2Cl_2 and I) THF inside.

volume of DCM molecules is smaller than the space of cavity. Thus, the DCM molecules can undergo uncontrollable molecular motions during the single crystal X-ray diffraction analysis. However, no such behavior was observed in THF-encapsulated crystal mostly due to the volume matching between the host and the guest.

The packing information of TPP-*o*-TPE in both crystals is further investigated. In case of DCM-containing crystals, every four molecules coordinately form a cylinder-like pore with radius (r) and height (h) of ≈3.1 and 9 Å, respectively, with the aid of their folded structures (Figure 8H). The pore volume is further calculated as ≈0.27 nm^3 and competent in accommodating two DCM molecules. Besides, the nanopores are uniformly distributed but highly oriented. For example, in Figure S39 (Supporting Information), the nanopores arrange and connect almost in a straight line, indicative of the formation of long-range nanochannels. As shown above, the TPP-*o*-TPE crystals obtained in THF/methanol mixture adopt a molecular conformation similar to that obtained in DCM/methanol mixture. Does it imply that they possess a similar ability to capture THF molecules? The answer is yes. Indeed, the analogous nanopores with cylinder shape are generated by incorporating two THF molecules (Figure 8I). Because the size of THF molecules is much larger than DCM, the pore thus has longer r and h of ≈3.5 and 11 Å and a larger volume of ≈0.42 nm^3. Besides, nanochannels are also formed along a certain direction (Figure S40, Supporting Information). All these indicate that TPP-*o*-TPE is apt to form porous crystals by virtue of its folded conformation caused by the isomerism effect. The intramolecular C—H...N hydrogen bond existed in the crystals helps to fix the solid geometry of TPP-*o*-TPE, thus providing a definitive manner to construct pore structure. However, the volume of nanopores in the porous crystals is still tunable in consideration of different sizes of the guest molecules.

3. Conclusions

In this contribution, we synthesized three AIE isomers, named TPP-*p*-TPE, TPP-*m*-TPE, and TPP-*o*-TPE, by connecting TPE to TPP at the *para*-, *meta*-, and *ortho*-positions, respectively. The isomerism effect of AIEgens leads to some obvious difference in the luminescence behavior and solid-state property during conformational changes to direct to various applications. For example, the stretching structure of AIEgen enables it to possess the best conjugation and tight packing in the aggregation state, making the molecules to emit efficiently in the film state and possess enhanced interactions with analytes suitable for OLED and nanoprobe applications. However, slightly bending the structure of AIEgen will shorten its conjugation length and induce deep-blue emission. The fabricated device emits a much pure blue light but at the expense of performances due to its decreased luminescence efficiency and loose packing in the aggregate state. The folded structure of AIEgens enables them to form porous nanoaggregates, which show low emission efficiency but improved sensitivity as fluorescent probes. The folded conformation also led them easy to assemble into porous crystals with similar structure but produce different pore volume to capture different guest molecules. All these results indicate that the study of isomerism effect of AIEgens is instructive for precise control of material properties, which

© 2019 WILEY-VCH Verlag GmbH & Co. KGaA, Weinheim

provides useful information for developing functional materials with high performance.

4. Experimental Section

Materials and Instrumentation: All the commercially available chemicals were purchased from Sigma-Aldrich or Energy Chemical and used directly without further purification. 2-(4-Bromophenyl)-3,5,6-triphenylpyrazine was synthesized according to the previous report.[11d] THF was distilled from sodium benzopheone ketyl under dry nitrogen immediately prior to use. ^{1}H and ^{13}C spectra were recorded on a Bruker AVIII 400 MHz NMR spectrometer using $CDCl_3$ or CD_2Cl_2 as solvent. High-resolution mass spectra (HRMS) were measured with a GCT premier CAB048 mass spectrometer operated in MALDI-TOF mode. UV–visible absorption spectra were performed on a Cary 50 Conc spectrophotometer. PL spectra were recorded on a HORIBA spectrofluorometer. The absolute Φ_F values were measured with a Hamamatsu Quantaurus-QY C11347 spectrometer. The PL decay curves were recorded using an Edinburgh FLSP920 fluorescence spectrophotometer equipped with a xenon laser arc lamp (Xe900), a microsecond flash lamp (uF900), a picosecond pulsed diode laser (EPL-375), and a closed-cycle cryostate (CS202*I-DMX-1SS, Advanced Research Systems). TGA was carried out on a TA TGA Q5000 under nitrogen at a heating rate of 10 °C min^{-1}. DSC was performed on a TA DSC Q1000 under nitrogen at a heating rate of 10 °C min^{-1}. Cyclic voltammetry was performed at room temperature in a three-electrode cell using CHI610E electrochemical workstation. Electrochemical investigations were carried out in anhydrous CH_2Cl_2 with Pt disk, Pt wire, and saturated calomel electrode as working electrode, auxiliary electrode, and reference electrode, respectively. 0.1 M *n*-tetrabutylammonium hexafluorophosphate and ferrocene were used as supporting electrolyte and standard, respectively. The electrolyte solution was purged with nitrogen before measurements and the scanning rates were 50 mV s^{-1}.

*Synthesis of 2-(3-bromophenyl)-1-Phenylethanone (**1**)*: The product was prepared according to the literature.[21] Into a 500 mL round bottom flask was added 21.5 g (100 mmol) of 3-bromophenylacetic acid and 14.6 mL (200 mmol) of thionyl chloride. The mixture was stirred under reflux for 3 h. Afterward, the residual thionyl chloride was removed by reduced pressure. The crude product was dissolved in 200 mL of dichloromethane, followed by adding 11.52 mL (130 mmol) of benzene. Then, 17.4 g (130 mmol) of anhydrous $AlCl_3$ was added in portion at 0 °C and the solution was stirred for 1 h. The mixture was poured onto ice water and was extracted by dichloromethane. The organic phase was washed with water several times and condensed under reduced pressure. The crude product was purified on a silica-gel column using hexane/ethyl acetate mixture (v/v = 20:1) as eluent. A white powder of 21.2 g (77 mmol) was obtained in a yield of 77%. ^{1}H NMR (400 MHz, $CDCl_3$), δ (ppm): 7.98–7.96 (m, 2H), 7.56–7.52 (t, 1H), 7.45–7.40 (m, 3H), 7.37–7.34 (m, 1H), 7.16–7.14 (2H), 4.21 (s, 2H). ^{13}C NMR (100 MHz, $CDCl_3$), δ (ppm): 196.2, 136.2, 135.8, 132.9, 132.0, 129.6, 129.5, 128.2, 128.0, 127.8, 122.0, 44.2.

*Synthesis of 1-(3-bromophenyl)-2-Phenylethane-1,2-Dione (**2**)*: The product was prepared according to the literature.[22] Into a 500 mL round bottom flask was added 16 g (58.2 mmol) of **1**, 108 mL of dimethyl sulfoxide, 54 mL of water and 108 mL of HBr in acetic acid (33 wt%). The mixture was stirred at 100 °C overnight. Afterward, the mixture was cooled to room temperature, poured onto ice water and extracted with the ethyl acetate several times. The organic phase was washed with water several times and condensed under reduced pressure. The crude product was purified on a silica-gel column using hexane/ethyl acetate mixture (v/v = 20:1) as eluent. A yellow solid of 16.7 g (57.8 mmol) was obtained in a yield of 99.3%. ^{1}H NMR (400 MHz, $CDCl_3$), δ (ppm): 8.15–8.14 (t, 1H), 7.99–7.97 (m, 2H), 7.91–7.88 (m, 1H), 7.81–7.78 (m, 1H), 7.71–7.67 (m, 1H), 7.56–7.52 (t, 2H), 7.42–7.38 (t, 1H). ^{13}C NMR (100 MHz, $CDCl_3$), δ (ppm): 192.9, 192.2, 137.1, 134.6, 134.1, 132.0, 131.9, 130.0, 129.4, 128.5, 128.0, 122.7.

*Synthesis of 2-(3-bromophenyl)-3,5,6-Triphenylpyrazine (**3**)*: Into a 250 mL round bottom flask was added 15.5 g (53.6 mmol) of **2**, 13.7 g (64.4 mmol) of 1,2-diphenylethane-1,2-diamine, and 80 mL of acetic acid. The mixture was stirred under reflux for 4 h. Afterward, the mixture was cooled to room temperature and the powder was collected by filtration. The crude product was further recrystallized in acetic acid. A pale-yellow powder of 17.5 g (37.8 mmol) was obtained in a yield of 70%. ^{1}H NMR (400 MHz, $CDCl_3$), δ (ppm): 7.95–7.94 (t, 1H), 7.65–7.62 (m, 6H), 7.47–7.45 (m, 1H), 7.42–7.40 (m, 1H), 7.37–7.32 (m, 9H), 7.14–7.10 (t, 1H). ^{13}C NMR (100 MHz, $CDCl_3$), δ (ppm): 148.4, 148.0, 147.9, 146.2, 139.9, 137.6, 137.4, 132.1, 131.0, 129.3, 128.9, 128.3, 128.2, 127.9, 127.8, 127.7, 121.9.

*Synthesis of 2-(2-bromophenyl)-1-Phenylethanone (**4**)*: The synthetic procedure was similar to that of **1**. A white powder of 9.4 g (34.2 mmol) was obtained in a yield of 68.3%. ^{1}H NMR (400 MHz, $CDCl_3$), δ (ppm): 8.07-8.05 (m, 2H), 7.61–7.58 (m, 2H), 7.51–7.48 (m, 2H), 7.31–7.24 (m, 2H), 7.17–7.13 (m, 1H), 4.46 (s, 2H). ^{13}C NMR (100 MHz, $CDCl_3$), δ (ppm): 195.7, 136.0, 134.4, 132.7, 132.2, 131.1, 128.1, 127.7, 126.9, 124.5, 45.2.

*Synthesis of 1-(2-bromophenyl)-2-Phenylethane-1,2-Dione (**5**)*: The synthetic procedure was similar to that of 2. A yellow viscous liquid of 9.1 g (31.5 mmol) was obtained in a yield of 94.6%. ^{1}H NMR (400 MHz, $CDCl_3$), δ (ppm): 8.10–8.07 (m. 2H), 7.84–7.82 (m, 1H), 7.70–7.63 (m, 2H), 7.57–7.43 (m, 4H). ^{13}C NMR (100 MHz, $CDCl_3$), δ (ppm): 193.6, 190.9, 135.4, 133.9, 133.8, 133.1, 132.1, 131.9, 129.7, 128.3, 127.2, 121.2.

*Synthesis of 2-(2-bromophenyl)-3,5,6-Triphenylpyrazine (**6**)*: The synthetic procedure was similar to that of **3**. A pale-yellow powder of 9.5 g (20.5 mmol) was obtained in a yield of 68%. ^{1}H NMR (400 MHz, $CDCl_3$), δ (ppm): 7.66–7.63 (m, 2H), 7.61–7.56 (m, 5H), 7.51–7.48 (m, 1H), 7.36–7.21 (m, 11H). ^{13}C NMR (100 MHz, $CDCl_3$), δ (ppm): 149.6, 149.1, 148.5, 148.4, 139.3, 137.8, 137.7, 137.2, 132.5, 131.5, 129.4, 129.3, 128.9, 128.1, 128.0, 127.7, 127.6, 127.4, 126.9, 122.4.

*Synthesis of 2,3,5-Triphenyl-6-(2-(4,4,5,5-tetramethyl-1,3,2-dioxaborolan-2-yl)phenyl) Pyrazine (**7**)*: Into a 100 mL round bottom flask was added 2 g (4.3 mmol) of **6** and 50 mL of dry tetrahydrofuran under nitrogen. The system was cooled to −78 °C and then 4.3 mL (8.6 mmol) of *n*-BuLi solution (2 M) was injected dropwise. After stirring at −78 °C for 1 h, 2.6 mL (12.9 mmol) of 2-isopropoxy-4,4,5,5-tetramethyl-1,3,2-dioxaborolane was added. The reaction was warmed to room temperature and stirred overnight. Then, aqueous solution of NH_4Cl was added to quench the reaction and the mixture was extracted with dichloromethane. The organic phase was washed with water several times and condensed under reduced pressure. The crude product was purified on a silica-gel column using hexane/dichloromethane mixture (v/v = 2:1) as eluent. A white powder of 1.26 g (2.47 mmol) was obtained in a yield of 57.4%. ^{1}H NMR (400 MHz, $CDCl_3$), δ (ppm): 7.82–7.80 (d, 1H), 7.69–7.65 (m, 4H), 7.60–7.58 (m, 2H), 7.36–7.32 (m, 4H), 7.27–7.24 (m, 7H), 7.21–7.19 (d, 1H), 0.99 (s, 12H). ^{13}C NMR (100 MHz, $CDCl_3$), δ (ppm): 150.3, 148.0, 147.9, 144.3, 138.3, 138.1, 137.7, 134.3, 129.5, 129.3, 129.1, 127.8, 127.7, 127.6, 127.5, 127.4, 126.9, 82.9, 24.1.

Synthesis of TPP-p-TPE: Into a 250 mL round bottom flask was added 500 mg (1.08 mmol) of 2-(4-bromophenyl)-3,5,6-triphenylpyrazine, 495 mg (1.3 mmol) of 4,4,5,5-tetramethyl-2-(1,2,2-triphenylvinyl)-1,3,2-dioxaborolane, 62 mg (0.05 mmol) of $Pd(PPh_3)_4$, and 60 mL of dry tetrahydrofuran under nitrogen. After the mixture was dissolved, 30 mL of 2 M aqueous solution of K_2CO_3 was injected. The mixture was stirred at 80 °C overnight. Afterward, the mixture was extracted with dichloromethane. The organic phase was washed by water several times and condensed under reduced pressure. The crude product was purified on a silica-gel column using hexane/dichloromethane mixture (v/v = 10:1) as eluent. A white powder of 440 mg (0.69 mmol) was obtained in a yield of 63.9%. ^{1}H NMR (400 MHz, $CDCl_3$), δ (ppm): 7.62–7.60 (m, 6H), 7.39–7.37 (d, 2H), 7.33–7.31 (m, 9H), 7.16–7.04 (m, 15H), 7.00–6.98 (d, 2H). ^{13}C NMR (100 MHz, $CDCl_3$), δ (ppm): 148.4, 148.3, 144.3, 143.6, 143.4, 141.2, 140.3, 138.2, 136.3, 131.4, 131.3, 131.2, 129.9, 129.3, 128.6, 128.2, 127.7, 126.7, 126.6. HRMS (MALDI-TOF): *m/z* 638.2754 ([M]$^+$), calcd for $C_{48}H_{34}N_2$ 638.2722).

© 2019 WILEY-VCH Verlag GmbH & Co. KGaA, Weinheim

Synthesis of TPP-m-TPE: The synthetic procedure was similar to that of TPP-*p*-TPE except bromine-substituted derivative was replaced by **3**. A white powder of 510 mg (0.8 mmol) was obtained in a yield of 74.1%. ^{1}H NMR (400 MHz, $CDCl_3$), δ (ppm): 7.60–7.56 (m, 4H), 7.49–7.47 (m, 2H), 7.36–7.29 (m, 11H), 7.18–7.12 (m, 3H), 7.09–6.96 (m, 14H). ^{13}C NMR (100 MHz, $CDCl_3$), δ (ppm): 148.6, 148.4, 148.2, 144.0, 143.6, 143.5, 143.2, 141.2, 140.6, 138.6, 138.5, 138.3, 132.6, 131.5, 131.3, 131.2, 130.0, 129.9, 128.6, 128.5, 128.2, 128.1, 127.7, 127.6, 126.5, 126.4. HRMS (MALDI-TOF): *m*/*z* 638.2710 ([M]$^+$), calcd for $C_{48}H_{34}N_2$ 638.2722).

Synthesis of TPP-o-TPE: The synthetic procedure was similar to that of TPP-*p*-TPE except bromine and boron ester-substituted derivatives were replaced by bromotriphenylethylene and **7**. A white powder of 80 mg (0.13 mmol) was obtained in a yield of 19.3%. ^{1}H NMR (400 MHz, CD_2Cl_2), δ (ppm): 7.56–7.54 (m, 4H), 7.36–6.93 (m, 23H), 6.84–6.83 (m, 3H), 6.78–6.76 (d, 2H), 6.70 (d, 2H). ^{13}C NMR (100 MHz, CD_2Cl_2), δ (ppm): 145.8, 145.7, 145.6, 140.7, 140.2, 135.8, 132.6, 131.0, 130.7, 130.1, 129.8, 128.5, 128.3, 128.0, 127.8, 127.4, 127.0, 126.4, 126.2, 126.0, 125.8. HRMS (MALDI-TOF): *m*/*z* 638.2758 ([M]$^+$), calcd for $C_{48}H_{34}N_2$ 638.2722).

Fabrication of OLEDs: Multilayer OLEDs were fabricated by the vacuum-deposition method. Organic layers were deposited by high-vacuum (5×10^{-4} Pa) thermal evaporation onto a glass substrate pre-coated with a 90 nm indium tin oxide (ITO) layer, which was thoroughly cleaned and treated by O_2 plasma before conducting experiments. All organic layers were deposited sequentially. *N,N′*-di(1-naphthyl)-*N,N′*-diphenyl-benzidine (NPB) was used as the hole-transporting layer (HTL). TPBi was used as the electron-transporting layer (ETL) and LiF/Al was used as the cathode. The thermal deposition rates for the organic materials, LiF, and Al were 1.0, 0.1, and 3 Å s^{-1}, respectively. The active area of each device was 9 mm^2. The electroluminescence spectra, current density–voltage–luminance (*J*–*V*–*L*) characteristics, and the electroluminescence spectra of the OLEDs were carried out with a Photo Research SpectraScan PR-745 Spectroradiometer and a Keithley 2450 Source Meter and they were recorded simultaneously. All measurements were done at room temperature under ambient conditions.

Detection of PA and Ru^{3+}: The detections were carried out by adding the aqueous solution of PA and Ru^{3+} with different concentrations into the THF solution of AIEgens in volume ratio of 9:1. [CCDC 1915439 (TPP-*p*-TPE), 1915441 (TPP-*o*-TPE·DCM), and 1915442 (TPP-*o*-TPE·THF) contain the supplementary crystallographic data for this paper. These data can be obtained free of charge from The Cambridge Crystallographic Data Centre via www.ccdc.cam.ac.uk/data_request/cif.]

Supporting Information

Supporting Information is available from the Wiley Online Library or from the author.

Acknowledgements

This work was partially supported by the National Natural Science Foundation of China (21788102), the University Grants Committee of Hong Kong (AoE/P-03/08), the Research Grants Council of Hong Kong (16305015, A-HKUST 605/16 and C6009-17G), the Innovation and Technology Commission (ITC-CNERC14SC01 and ITCPD/17-9), and the Science and Technology Plan of Shenzhen (JCYJ20170818113602462 and JCYJ20160229205601482).

Conflict of Interest

The authors declare no conflict of interest.

Keywords

aggregation-induced emission, isomerism effect, nanofluorescent probes, organic light-emitting diodes, porous crystals

Received: May 14, 2019
Revised: June 19, 2019
Published online:

[1] a) C. Wang, H. Dong, W. Hu, Y. Liu, D. Zhu, *Chem. Rev.* **2012**, *112*, 2208; b) O. Ostroverkhova, *Chem. Rev.* **2016**, *116*, 13279; c) D. Li, W. Y. Lai, Y. Z. Zhang, W. Huang, *Adv. Mater.* **2018**, *30*, 1704738; d) Y. Xu, S. Jin, H. Xu, A. Nagai, D. Jiang, *Chem. Soc. Rev.* **2013**, *42*, 8012; e) M. Sessolo, H. J. Bolink, *Adv. Mater.* **2011**, *23*, 1829; f) H. C. Zhou, J. R. Long, O. M. Yaghi, *Chem. Rev.* **2012**, *112*, 673.

[2] a) P. Zhang, W. Dou, Z. Ju, X. Tang, W Liu, C. Chen, B. Wang, W. Liu, *Adv. Mater.* **2013**, *25*, 6112; b) Q. Qi, J. Qian, X. Tian, J. Zhang, L. Wang, B. Xu, B. Zou, W. Tian, *Adv. Funct. Mater.* **2015**, *25*, 4174; c) H. J. Kim, D. R. Whang, J. Gierschner, S. Y. Park, *Angew. Chem., Int. Ed.* **2016**, *55*, 15915.

[3] a) J. Mei, Y. Diao, A. L. Appleton, L. Fang, Z. Bao, *J. Am. Chem. Soc.* **2013**, *135*, 6724; b) J. Wang, M. Chu, J. X. Fan, T. K. Lau, A. M. Ren, X. Liu, Q. Miao, *J. Am. Chem. Soc.* **2019**, *141*, 3589; c) S. Casalini, C. A. Bortolotti, F. Leonardi, F. Biscarini, *Chem. Soc. Rev.* **2017**, *46*, 40.

[4] J. B. Birks, *Photophysics of Aromatic Molecules*, Wiley, London **1970**.

[5] a) J. M. Kang, H. J. Cho, J. Lee, J. I. Lee, S. K. Lee, N. S. Cho, D. H. Hwang, H. K. Shim, *Macromoelcules* **2006**, *39*, 4999; b) S. Xiao, M. Nguyen, X. Gong, Y. Cao, H. Wu, D. Moses, A. J. Heeger, *Adv. Funct. Mater.* **2003**, *13*, 25; c) Y. Zou, J. Zou, T. Ye, H. Li, C. Yang, H. Wu, D. Ma, J. Qin, Y. Cao, *Adv. Funct. Mater.* **2012**, *23*, 1781.

[6] a) G. Niu, R. Zhang, J. P. C. Kwong, J. W. Y. Lam, C. Chen, J. Wang, Y. Chen, X. Feng, R. T. K. Kwok, H. H.-Y. Sung, I. D. Williams, M. R. J. Elsegood, J. Qu, C. Ma, K. S. Wong, X. Yu, B. Z. Tang, *Chem. Mater.* **2018**, *30*, 4778; b) P. Wei, J. X. Zhang, Z. Zhao, Y. Chen, X. He, M. Chen, J. Gong, H. H.-Y Sung, I. D. Williams, J. W. Y. Lam, B. Z. Tang, *J. Am. Chem. Soc.* **2018**, *140*, 1966; c) Y. C. Duan, Y. Gao, Y. Geng, Y. Wu, G. G. Shan, L. Zhao, M. Zhang, Z. M. Su, *J. Mater. Chem. C* **2019**, *7*, 2699; d) W. Fu, C. Yan, Z. Guo, J. Zhang, H. Zhang, H. Tian, W. H. Zhu, *J. Am. Chem. Soc.* **2019**, *141*, 3171; e) S. Chen, P. Zeng, W. Wang, X. Wang, Y. Wu, P. Lin, Z. Peng, *J. Mater. Chem. C* **2019**, *7*, 2886; f) Z. Chi, X. Zhang, B. Xu, X. Zhou, C. Ma, Y. Zhang, S. Liu, J. Xiu, *Chem. Soc. Rev.* **2012**, *41*, 3878.

[7] a) J. Mei, N. L. C. Leung, R. T. K. Kwok, J. W. Y. Lam, B. Z. Tang, *Chem. Rev.* **2015**, *115*, 11718; b) D. Ding, K. Li, B. Liu, B. Z. Tang, *Acc. Chem. Res.* **2013**, *46*, 2441.

[8] J. Wang, J. Mei, E. Zhao, Z. Song, A. Qin, J. Z. Sun, B. Z. Tang, *Macromolecules* **2012**, *45*, 7692.

[9] J. Mei, J Wang, A. Qin, H. Zhao, W. Yuan, Z. Zhao, H. H. Y. Sung, C. Deng, S. Zhang, I. D. Williams, J. Z. Sun, B. Z. Tang, *J. Mater. Chem.* **2012**, *22*, 4290.

[10] a) Z. Zhao, C. Chen, W. Wu, F. Wang, L. Du, X. Zhang, Y. Xiong, X. He, Y. Cai, R. T. K. Kwok, J. W. Y. Lam, X. Gao, P. Sun, D. L. Phillips, D. Ding, B. Z. Tang, *Nat. Commun.* **2019**, *10*, 768; b) P. Alam, N. L. C. Leung, Y. Cheng, H. Zhang, J. Liu, W. Wu, R. T. K. Kwok, J. W. Y. Lam, H. H. Y. Sung, I. D. Williams, B. Z. Tang, *Angew. Chem., Int. Ed.* **2019**, *58*, 4536.

[11] a) M. Chen, L. Li, H. Nie, J. Tong, L. Yan, B. Xu, J. Z. Sun, W. Tian, Z. Zhao, A. Qin, B. Z. Tang, *Chem. Sci.* **2016**, *6*, 1932; b) M. Chen, R. Chen, Y. Shi, J. Wang, Y. Cheng, Y. Li, X. Gao, Y. Yan, J. Z. Sun, A. Qin, R. T. K. Kwok, J. W. Y. Lam, B. Z. Tang, *Adv. Funct. Mater.* **2018**, *28*, 1704689; c) M. Chen, L. Li, H. Wu, L. Pan, S. Li, B. He, H. Zhang, J. Z. Sun, A. Qin, B. Z. Tang, *ACS Appl. Mater. Interfaces*

 © 2019 WILEY-VCH Verlag GmbH & Co. KGaA, Weinheim

2018, *10*, 12181; d) M. Chen, H. Nie, B. Song, L. Li, J. Z. Sun, A. Qin, B. Z. Tang, *J. Mater. Chem. C* **2016**, *4*, 2901; e) Y. Jiang, L. Sun, J. Du, Y. Liu, H. Shi, Z. Liang, J. Li, *Cryst. Growth Des.* **2017**, *17*, 2090; f) H. Li, Z. Chi, X. Zhang, B. Xu, S. Liu, Y. Zhang, J. Xu, *Chem. Commun.* **2011**, *47*, 11273; g) H. Li, X. Zhang, Z. Chi, B. Xu, W. Zhou, S. Liu, Y. Zhang, J. Xu, *Org. Lett.* **2011**, *4*, 556.

[12] a) J. Hu, Q. Li, X. Wang, S. Shao, L. Wang, X. Jing, F. Wang, *Angew. Chem., Int. Ed.* **2019**, *58*, 8405; b) X. Wang, S. Wang, J. Lv, S. Shao, L. Wang, X. Jing, F. Wang, *Chem. Sci.* **2019**, *10*, 2915; c) H. Pan, G. Fu, Y. Zhao, C. Zhao, *Org. Lett.* **2011**, *13*, 4830; d) P. Zhang, J. Zeng, J. Guo, S. Zhen, B. Xiao, Z. Wang, Z. Zhao, B. Z. Tang, *Front. Chem.* **2019**, *7*, 199.

[13] a) R. Misra, T. Jadhav, B. Dhokale, S. M. Mobin, *Chem. Commun.* **2014**, *50*, 9076; b) T. Jimbo, M. Tsuji, R. Taniguchi, K. Sada, K. Kokado, *Cryst. Growth Des.* **2018**, *18*, 3863; c) M. Z. K. Baig, B. Prusti, M. Chakravarty, *J. Mater. Chem. C* **2019**, *7*, 3735; d) M. Desroches, J. F. Morin, *Org. Lett.* **2018**, *20*, 2797; e) J. Huang, N. Sun, Y. Dong, R. Tang, P. Lu, P. Cai, Q. Li, D. Ma, J. Qin, Z. Li, *Adv. Funct. Mater.* **2013**, *23*, 2329; f) W. Huang, M. Bender, K. Seehafer, I. Wacker, R. R. Schröder, U. H. F Bunz, *Macromolecules* **2018**, *51*, 1345.

[14] a) T. Fleetham, G. Li, L. Wen, J. Li, *Adv. Mater.* **2014**, *26*, 7116; b) Q. Zhang, J. Li, K. Shizu, S. Huang, S. Hirata, H. Miyazaki, C. Adachi, *J. Am. Chem. Soc.* **2012**, *134*, 14706; c) S. Tao, Y. Zhou, C. S. Lee, X. Zhang, S. T. Lee, *Chem. Mater.* **2010**, *22*, 2138; d) X. Cai, S. J. Su, *Adv. Funct. Mater.* **2018**, *28*, 1802558; e) J. Y. Hu, Y. J. Pu, F. Satoh, S. Kawata, H. Katagiri, H. Sasabe, J. Kido, *Adv. Funct. Mater.* **2014**, *24*, 2064.

[15] a) C. W. Tang, S. A. VanSlyke, *Appl. Phys. Lett.* **1987**, *51*, 913; b) G. G. Malliaras, J. R. Salem, P. J. Brock, C. Scott, *Phys. Rev. B* **1998**, *58*, R13411.

[16] J. Liu, Y. Zhong, J. W. Y. Lam, P. Lu, Y. Hong, Y. Yu, Y. Yue, M. Faisal, H. H. Y. Sung, I. D. Williams, K. S. Wong, B. Z. Tang, *Macromolecules* **2010**, *43*, 4921.

[17] a) L. K. Fraiji, D. M. Hayes, T. C. Werner, *J. Chem. Educ.* **1992**, *69*, 424; b) J. R. Barrio, G. L. Tolman, N. J. Leonard, R. D. Spencer, G. Weber, *Proc. Natl. Acad. Sci. USA* **1973**, *70*, 941; c) E. R. Carraway, J. N. Demas, *Anal. Chem.* **1991**, *63*, 332.

[18] a) P. Suresh, I. A. Azath, K. Pitchumani, *Sens. Actuators, B* **2010**, *146*, 273; b) V. Muthukumar, S. K. Iyer, *Sens. Actuators, B* **2018**, *267*, 373.

[19] a) C. Y. K. Chan, J. W. Y. Lam, C. K. W. Jim, H. H. Y. Sung, I. D. Williams, B. Z. Tang, *Macromolecules* **2013**, *46*, 9494; b) H. Deng, R. Hu, E. Zhao, C. Y. K. Chan, J. W. Y. Lam, B. Z. Tang, *Macromolecules* **2014**, *47*, 4902.

[20] a) P. P. H. Cheng, D. Silester, G. Wang, G. Kalyuzhny, A. Douglas, R. W. Murray, *J. Phys. Chem. B* **2006**, *110*, 4637; b) C. A. M. Seidel, *J. Phys. Chem.* **1996**, *100*, 5541.

[21] J. W. Yu, S. Mao, Y. Q. Wang, *Tetrahedron Lett.* **2015**, *56*, 1575.

[22] M.-A. Tehfe, F. Dumur, B. Graff, J.-L. Clément, D. Gigmes, F. Morlet-Savary, J.-P. Fouassier, J. Lalevée, *Macromolecules* **2013**, *46*, 736.

© 2019 WILEY-VCH Verlag GmbH & Co. KGaA, Weinheim